[논 문] 한국재료학회지
Korean J. Mater. Res.
Vol. 30, No. 7 (2020)
https://doi.org/10.3740/MRSK.2020.30.7.333

Fabrication and Electrical Transport Characteristics of All-Perovskite Oxide $DyMnO_3$ / Nb-1.0 wt% Doped $SrTiO_3$ Heterostructures

Wei Tian Wang†

Institute of Opto-Electronic Information Science and Technology, Yantai University, Yantai 264005, P.R. China

(Received May 6, 2020 : Revised July 3, 2020 : Accepted July 7, 2020)

Abstract Orthorhombic $DyMnO_3$ films are fabricated epitaxially on Nb-1.0 wt%-doped $SrTiO_3$ single crystal substrates using pulsed laser deposition technique. The structure of the deposited $DyMnO_3$ films is studied by X-ray diffraction, and the epitaxial relationship between the film and the substrate is determined. The electrical transport properties reveal the diodelike rectifying behaviors in the all-perovskite oxide junctions over a wide temperature range (100 ~ 340 K). The forward current is exponentially related to the forward bias voltage, and the extracted ideality factors show distinct transport mechanisms in high and low positive regions. The leakage current increases with increasing reverse bias voltage, and the breakdown voltage decreases with decrease temperature, a consequence of tunneling effects because the leakage current at low temperature is larger than that at high temperature. The determined built-in potentials are 0.37 V in the low bias region, and 0.11 V in the high bias region, respectively. The results show the importance of temperature and applied bias in determining the electrical transport characteristics of all-perovskite oxide heterostructures.

Key words perovskite, heterostructure, electrical transport, diodelike.

1. Introduction

Perovskite rare-earth oxides $RMnO_3$ (R = lanthanide) have attracted a lot of attentions due to their diverse properties such as (anti)ferromagneticity, ferroelectricity, and magneto- resistance effects.[1-3] Among these materials, $DyMnO_3$ (DMO) has prominent underlying intriguing physics because of its complicated crystalline structures. Generally, perovskite oxides $RMnO_3$ crystallize in two types of structures: orthorhombic and hexagonal.[4,5] The different structures are strongly dependent on the radius of the rare earth ions. For larger ionic size, $RMnO_3$ adopts an orthorhombic distorted perovskite structure, while for smaller rare earth cation, $RMnO_3$ tends to take a hexagonal structure. Because of the medium size of Dy^{3+} ions, DMO can be crystallized in either hexagonal or orthorhombic structures depending on the synthesis methods.[6]

As is known, pulsed laser deposition (PLD) is a useful technique to fabricate oxide thin films which can be crystallized into fixed structures depending on the lattice matching relationship between the substrates and the films. In this paper, we reported the fabrication of orthorhombic DMO films epitaxially grown on 1.0 wt% Nb-doped $SrTiO_3$ (NSTO) substrates by using PLD technique. The structural and electrical transport properties of the heterostructure were studied. The unexpected diodelike rectifying behaviors in the current-voltage (*IV*) measurements show the heterojunction effects. Two distinct transport mechanisms were determined in high and low forward bias voltage regions.

2. Experimental

The orthorhombic DMO thin films were fabricated by PLD using a Lambda Physic KrF excimer laser (λ = 248 nm). The ceramic DMO target was prepared through standard solid-state reaction process which was reported previously.[7] The energy density of the focused laser on the target is about 2.5 J/cm^2. The single crystals NSTO (001) (0.5 mm in thickness) were used as substrates which were held at 700 ^{o}C under oxygen pressure of 30 Pa during the process of PLD. After 30 min in situ annealing, the deposited thin films were cooled down to room temperature with a rate of -5 ^{o}C / minute. The thickness of the fabricated DMO thin films

†Corresponding author
E-Mail : whetwang@163.com (W.T. Wang , Yantai Univ.)

was determined to be about 150 nm by a surface profile measuring system. The structures of the deposited DMO films were studied by x-ray diffraction (XRD) with Cu Kα radiation at 1.54 Å. The azimuthal φ scans were recorded in order to assess the phase purity and the epitaxial relationship between the films and the substrates.

For *IV* measurements, an evaporated Au spot with an area of 0.2 mm^2 on the surface of DMO film was used as top electrode and the bottom electrode was an In pad (1 mm^2) pressed on the NSTO substrate to minimize the contact resistance. The *IV* curves were measured in a temperature range of 100~340 K by applying a pulsed dc bias across the heterostructures.

3. Results and Discussion

Figure 1 shows the typical *q*-2*q* XRD result of the DMO film grown on NSTO (001) substrate. As can be seen, besides the sharp (00*l*) diffraction peaks from the DMO thin film, no diffraction from randomly oriented grains or impurity phases can be detected from the x-ray pattern, suggesting that the prepared DMO thin film is in orthorhombic structure with a clear *c*-orientation on NSTO (001) substrate. The full-width-half-maximum (FWHM) values of the (002) reflection is about 0.4° indicating good out-of-plane texture. To investigate the in-plane texture of the films, the x-ray φ scans around the DMO (112) and NSTO (112) reflections were shown in the inset of Fig. 1. The fourfold symmetry peaks reveal that the film is in orthorhombic structure and well aligned with the substrate. Each φ scan peak of DMO (112) is equally 45° spaced between the neighboring φ scan peaks of NSTO (112), which suggests a 45° rotation between the film and substrate.

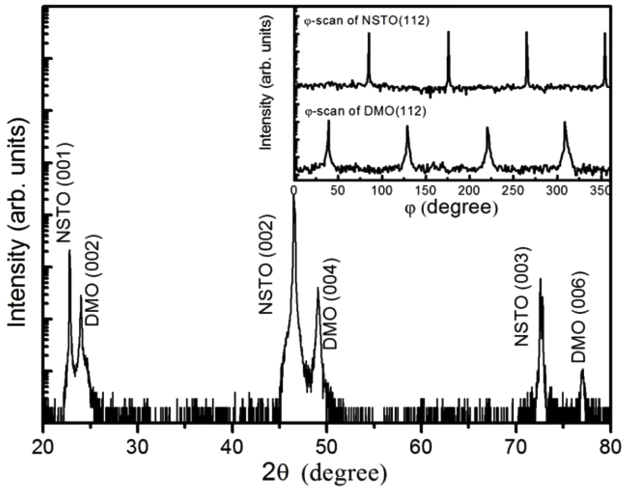

Fig. 1. Typical *θ*-2*θ* XRD pattern of DMO film on NSTO (001) substrate. The inset shows the φ scans of the (112) peaks of DMO film and NSTO substrate, displaying the well alignment of film with substrate.

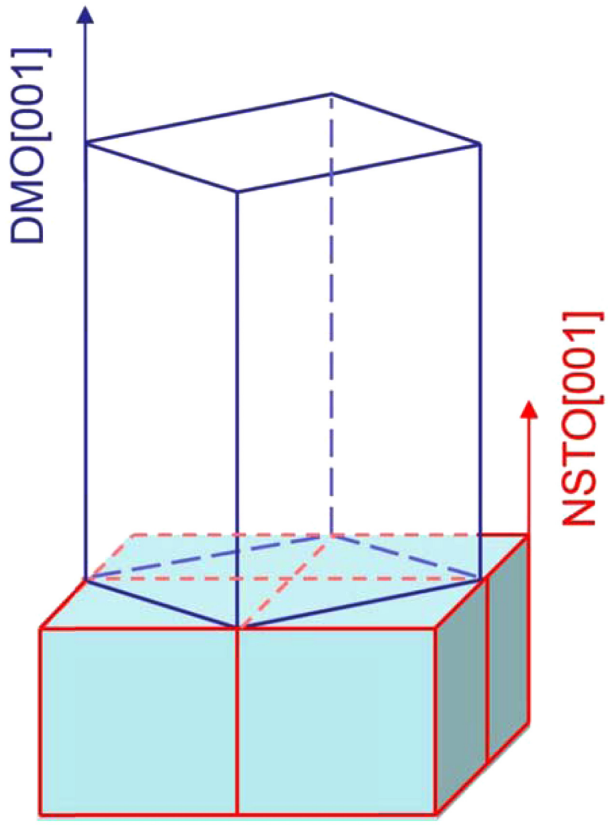

Fig. 2. The schematic diagram of epitaxial relationship between the DMO film and NSTO (001) substrate.

The in-plane epitaxial relationship can be determined as [001] DMO // [001] NSTO and [010] DMO // [110] NSTO.

The lattice parameters of the orthorhombic DMO are a =0.581 nm, b=0.527 nm and c=0.739 nm,[8] and the NSTO single crystal substrate is in cubic structure with lattice parameters of 0.3905 nm. The schematically display of DMO/NSTO (001) relationship is illustrated in Fig. 2. The lattice mismatches for the a- and b-parameters of DMO film with respect to the diagonal lines of the ab-plane of NSTO (001) substrate are expected to be -5.3 % along the [110] direction and 4.4 % along the [1$\underline{1}$0] direction of NSTO crystal. The calculation method of lattice mismatches was given in Ref. [9].

Figure 3 shows the *T* dependence of *IV* curves of DMO/NSTO (001) heterostructures. The schematic view of the sample geometry is shown in the upper set. Good diodelike behavior is evident in the temperature range investigated. The current is very small at reverse bias, while increases rapidly at forward bias. As shown in Fig. 3, the diffusion voltage increases monotonically with reducing *T* from 340 K to 100 K. Although, the stoichiometric manganate oxides are believed to behave as insulating materials, the rare-earth perovskite manganate films are reported to show the ability to accommodate more oxygen called

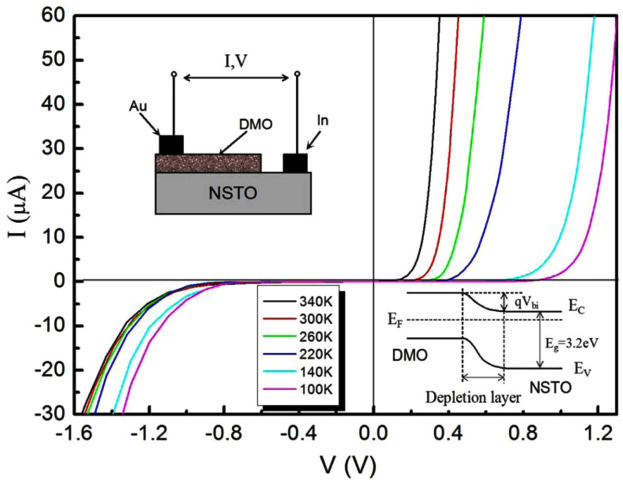

Fig. 3. Current-voltage (*IV*) characteristics of the DMO/NSTO heterojunction measured at different temperatures. Upper set: the sketch of the sample geometry for measurement. Lower set: schematic band diagram of the DMO/NSTO junction.

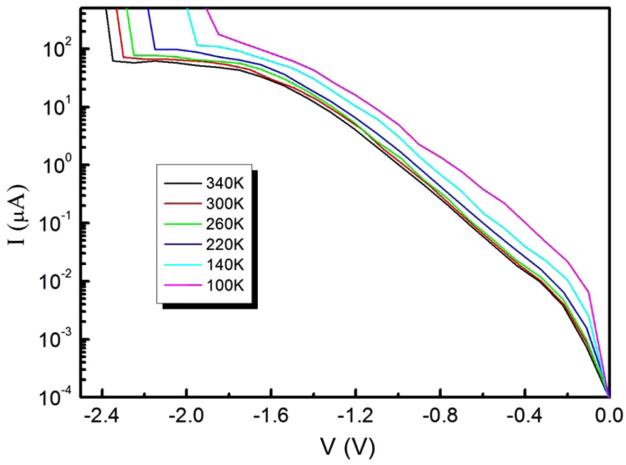

Fig. 4. Log scale of reverse leakage currents of DMO/NSTO at different temperatures.

"oxidation nonstoichiometry".[10,11] The excess oxygen might act as an acceptor, changing insulating DMO into a *p*-type semiconductor. Moreover, the large lattice mismatch between DMO film and NSTO substrate can lead to defects at the interface. The defects may result in metal vacancy, which will contribute to the transition of DMO film from the insulating to a hole-doped state.[12,13] In addition, NSTO substrate is reported as a degenerate *n*-type semiconductor with a donor density of ~ 5×10^{19} cm^{-3}.[14,15] Then the observed nonlinear *IV* electrical curves come from the DMO/NSTO heterojunctions. The band structure is schematically shown in the lower set of Fig. 3.

For clarity, the log scale of reverse leakage currents of DMO/NSTO (001) heterostructures at varying temperature is shown in Fig. 4. The leakage current rapidly increased with increasing reverse bias voltage. On the other hand, at the same reverse bias voltage, the leakage current increases with reducing *T* in the range of 340-100 K, which can be explained by tunneling through the heterojunctions. Similar results were reported in other all-perovskite oxide junctions.[15,16] As shown in Fig. 4, the breakdown voltage, at which an abrupt change in the reverse *IV* characteristics occurred, decreases with reducing *T*. The result is a consequence of tunneling effects as the leakage current at low temperature is larger than that at high temperature.

In abrupt *p*-*n* junction model, the forward current can be approximately described by exponential equations,[17]

$$I = I_s \exp\left(\frac{qV}{nk_BT}\right) \quad (1) \text{ and}$$

$$I_s = \gamma T \exp\left(-\frac{qV_{bi}}{k_BT}\right) \quad (2),$$

where V_{bi} is the built-in potential, I_s is the saturation current, q is the elementary charge, T is the junction temperature, n is the ideality factor, γ is a constant and V is the bias applied. As for the electrical transport in ideal heterojunction, n equals to 1. In practical devices, however, current transport is dominated by combination of many complex factors, which results in a larger value of n.

The exponential forward current in Fig. 3 can be well fitted by using equations (1) and (2). The results are shown in Fig. 5. The solid curves through the data points (open symbols) are the fitting results. There are two regions with different slopes of ln*I*-*V* curves at low and high forward biases in the temperature range, suggesting two different mechanisms for current transport. Figure 6 shows the extracted n in the two different regions. In low bias region, the obtained value of n is between 1 and 2 at

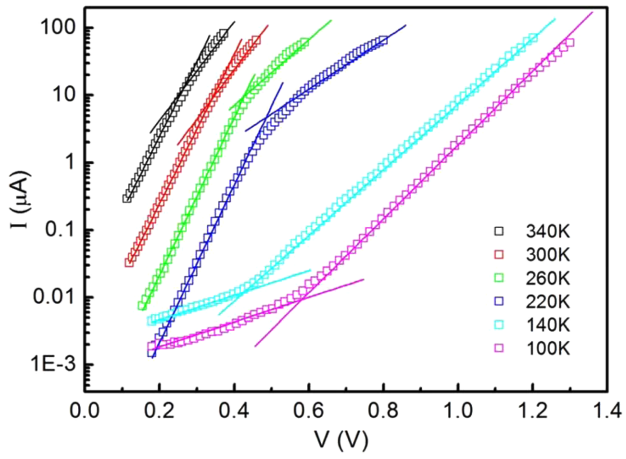

Fig. 5. Semilogarithmic plot of the forward bias region of *IV* characteristics of DMO/NSTO. The solid lines are theoretical fits.

high temperatures, which suggests that the current transport is dominated by diffusion. At low temperatures, below 220 K, the ideality factor reaches unphysical values, which implies that Eq. (1) is no longer applicable in such a situation. In high bias region, the obtained value of n is increased slowly as the temperature goes down, suggesting that the current transport is dominated by the recombination of charge carriers, and some other factors could contribute to the electrical transport at low temperatures. The temperature dependence of n is very commonly observed in p-n heterojunctions composed of oxides thin films,[18] which can be attributed to the inhomogeneities of the build-in potentials at the interfaces.[19,20]

According to equation (2), the semilogarithmic plot of I_s/T versus $1/T$ should give a straight line, and the slope indicates the build-in potentials. The results in low and high forward bias regions are shown in Fig. 7. The determined V_{bi} is 0.37 V in low bias region, and 0.11 V in high bias region. The different build-in potentials suggest that the applied forward bias has effects on the transport mechanisms.When T is below 220K in low bias region, the plot deviates from the straight line. The facts imply that equations (1) and (2) predicted by the thermionic emission model are no longer applicable. Because of the mismatch and interfacial stress distribution between the film and the substrate, the build-in potentials can vary with the applied electrical field. Moreover, many studies show that the dielectric properties of perovskite manganates are electrical field-dependent.[21] The permittivity variations of the films could cause the change of the build-in potentials at the interfaces.

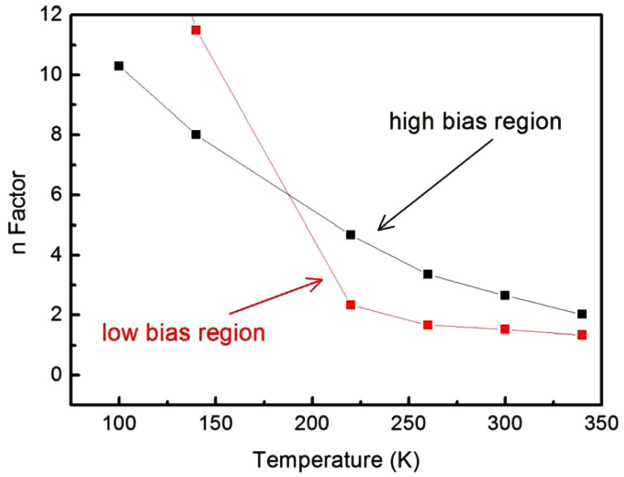

Fig. 6. The extracted ideality factor n in high and low forward bias regions.

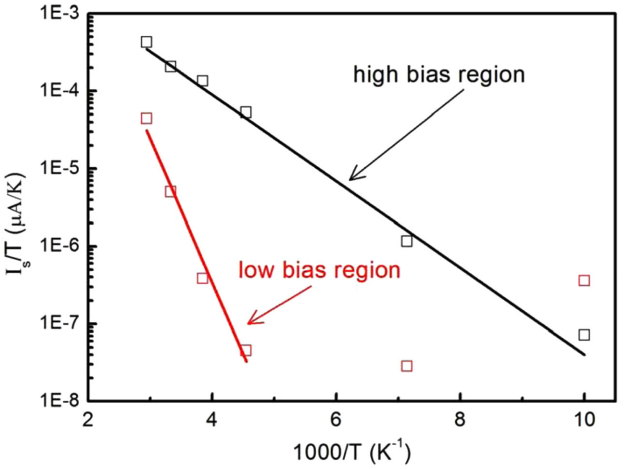

Fig. 7. Semilogarithmic plot of I_s/T versus $1/T$. The solid lines are linear fits.

4. Conclusion

In conclusion, orthorhombic DMO films were fabricated on NSTO (001) substrates by PLD technique. The crystal structure and the epitaxial relationship between the films and the substrates were analyzed. Electrical transport measurements show good rectifying behaviors in DMO / NSTO heterostructures. Two distinct transport mechanisms are identified. The forward current transport is dominated mainly by the recombination of charge carriers in high bias, and diffusion in low bias region respectively. The results underline the importance of temperature and applied bias in determining the electrical transport characteristics of all-perovskite oxide heterojunctions.

References

1. U. Dash and C.-U. Jung, J. Magn., **23**, 345 (2018).
2. S. Harikrishnan, S. Roßler, C. M. N. Kumar, H. L. Bhat, U. K. Roßler, S. Wirth, F. Steglich and S. Elizabeth, J. Phys.: Condens. Matter., **21,** 096002 (2009).
3. D. Ito, N. Fujimura, T. Yoshimura and T. Ito, J. Appl. Phys., **93**, 5563 (2003).
4. S. Jandl, S. Mansouri, A. A. Mukhin, V. Y. Ivanov, A. Balbashov, M. M. Gospodino, V. Nekvasil and M. Orlita, J. Magn. Magn. Mater., **323**, 1104 (2011).
5. V. Y. Ivanov, A. A. Mukhin, A. S. Prokhorov, A. M. Balbashov and L. D. Iskhakova, Phys. Solid State, **48**, 1726 (2006).
6. S. Remsen, B. Dabrowski, O. Chmaissem, J. Mais and A. Szewczyk, J. Solid State Chem., **184**, 2306 (2011).
7. W. T. Wang, Korean J. Mater. Res., **29**, 753 (2019).
8. K. Yadagiri, R. Nithya, N. Shukla and A.T. Satya, J. Alloys Compd., **695**, 2959 (2017).
9. A. A. Bosak, C. Dubourdieu, J. -P. Senateur , O. Y. Gorbenko and A. R. Kaul, Cryst. Eng., **5**, 355 (2002).
10. C. N. R. Rao and A. K. Cheetham, Science, **272**, 369 (1996).

11. R. Mahendiran, S. K. Tiwary, A.K. Raychadhuri, T. V. Ramakrisnan, R. Mahesh, N. Raganvittal and C. N. R. Rao, Phys. Rev. B: Condens. Matter Mater. Phys., **53**, 3348 (1996).
12. K. Chanara, T. Ohno, M. Kasai and Y. Kozono, Appl. Phys. Lett., **63**, 1990 (1993).
13. R. Von Helmolt, J. Wecker, B. Holzapfel, L. Schultz and K.Samwer, Phys. Rev. Lett., **71**, 2331 (1994).
14. M. Sugiura, K. Uragou, M. Noda, M. Tachiki and T. Kobayashi, Jpn. J. Appl. Phys., **38**, 2675 (1999).
15. Y. Watanabe, Phys. Rev. B: Condens. Matter Mater. Phys., **57**, R5563 (1998).
16. Y. M. Cui, L. W. Zhang, C. C. Wang, G. L. Xie, C. P. Chen and B. S. Cao, Appl. Phys. Lett., **86**, 203501 (2005).
17. F. Y. Bruno, J. Garcia-Barriocanal, M. Torija, A. Rivera, Z. Sefrioui, C. Leighton, C. Leon and J. Santamaria, Appl. Phys. Lett., **92**, 082106 (2008).
18. Y. Z. Chen, J. R. Sun, Y. W. Xie, D. J. Wang, W. M. Lu, S. Liang and B.G. Shen, Appl. Phys. Lett., **90**, 143508 (2007).
19. H. C. Casey, Jr., J. Muth, S. Krishnankutty and J. M. Zavada, Appl. Phys. Lett., **68**, 2867 (1996).
20. J. H. Werner and H. H. Guttler, J. Appl. Phys., **69**, 1522 (1991).
21. W. Wang, D. Yuan, Y. Sun and Y. Sun, J. Appl. Phys., **106**, 024106 (2009).

Author Information

Wei Tian Wang
Professor of physics in the Institute of Opto-Electronic Information Science and Technology, Yantai University, China.